Computational Study of Inclusion Complexes Formation between Metronidazole and *B*-Cyclodextrin: Dft, Nmr, Nbo, Aim, Nci-Rdg, and Igm Analysis

Dhouha Boulahraf, Amel Bendjeddou, Tahar Abbaz, Didier Villemin

Computational study of inclusion complexes formation between Metronidazole and *β*-cyclodextrin: DFT, NMR, NBO, AIM, NCI-RDG, and IGM analysis.

Dhouha Boulahraf[1,*], Amel Bendjeddou[1], Tahar Abbaz[1], and Didier Villemin[2]

[1] Laboratory of Organic Chemistry and Interdisciplinary, University of Souk Ahras, Souk Ahras, Algeria

[2] Laboratory of Molecular and Thio-Organic Chemistry, UMR CNRS 6507, INC3M, FR 3038, Labex EMC3, ensicaen & University of Caen, Caen 14050, France

Abstract: Metronidazole (MTZ) exhibits potent biological activity, but it has issues with its physicochemical and pharmacokinetic properties. These issues could be resolved and optimized by forming inclusion complexes with cyclodextrins. This work evaluates the interactions between MNZ and *β*-CD with 1:1 stoichiometry using various molecular modeling and computational methods. Two orientations of MNZ, A, and B, were considered. The techniques used include semi-empirical (PM3) and (DFT) calculations in gas and water using PW6B95, PW6B95D3, and B3LYP functional and 6-31G(d) basis sets. The results indicate that orientation A is more favorable than orientation B. In both orientations, metronidazole was completely embedded into the *β*-CD cavity. The Gauge-Including Atomic Orbital (GIAO) method was used to calculate 1H NMR shifts, which agreed well with experimental results. To better understand the intra- and intermolecular interactions between the host and the guest (*β*-CD and MNZ), an investigation was carried out using AIM, NBO, (RDG) NCI, and IGM analysis. The investigation confirmed the stability of the inclusion complex *β*-CD@MNZ due to H-bond and van der Waals interactions.

Keywords: *β*-cyclodextrin · metronidazole · DFT · NBO · QTAIM · NCI · IGM

1. Introduction

Encapsulation of hydrophobic or poorly soluble drugs by delivery systems can improve their aqueous solubility and chemical stability. One of these systems is cyclodextrin (CD) complexation technology, which has often been successful [1–2]. β-Cyclodextrin has a good cavity size, is less toxic, safer to administer, and more economical than other forms, making it ideal for complexation [3]. Metronidazole is an important antibiotic for the treatment of a wide range of infections and is

available in a variety of forms, including oral administration and topical applications [4–8]. However, its use in aqueous formulations is limited due to its low solubility in water [9]. It may cause side effects and carcinogenicity concerns with repeated oral use [7, 8]. To address these issues, researchers have been investigating the inclusion complex of metronidazole in cyclodextrin to improve the efficacy, stability, and water solubility of metronidazole for oral use [10, 11]. However, there are still some ambiguities regarding the mechanism of MNZ inclusion with *β*-Cyclodextrin that have not been examined. To gain a deeper understanding and evaluate the interactions and their nature in this inclusion complex MNZ@*β*-CD, a theoretical study using a high level of theory based on Density Functional Theory (DFT) calculations has been conducted. After determining the lowest energy structures using the semi-empirical method PM3, we compared PW6B95 (Perdew-Wang-91, 6-parameter functional exchange, and Becke-95 correlation), PW6B95-D3 (Perdew-Wang-91, 6-parameter functional exchange, and Becke-95 correlation with D3 Grimme's dispersion) [12], and B3LYP (Becke, 3-parameter, Lee-Yang-Parr) [13] with basis set 6-31G (d) for optimization in both gaseous and aqueous phases. In addition, we calculated complexation, interaction, and deformation energies, as well as frontier molecular orbitals (FMOs) and the global indices of reactivity. Using the GIAO approach, we systematically compared the calculated and experimentally measured ^{1}H NMR chemical shifts [10, 11]. Finally, the intra- and intermolecular interactions within the inclusion complex MNZ@*β*-CD were comprehensively analyzed using Natural Bond Orbital (NBO) analysis, Quantum Theory of Atoms in Molecules (QTAIM), Non-covalent Interactions-Reduced Density Gradient (NCI-RDG), and Independent Gradient Model (IGM) analysis.

2. Computational details:

The structures of *β*-cyclodextrin and metronidazole were obtained from PubChem [14]. The MNZ and *β*-CD inclusion structures were initially constructed using HyperChem version 8.0 [15]. Gaussian 16 [16] was employed for semi-empirical PM3 and high-level theoretical DFT calculations, including structure optimization, single-point energies, NBO, and NMR. The results were visualized using GaussView 6.0 [17]. The Multiwfn 3.8 software [18] was used to calculate the QTAIM, NCI, and IGM analyses, which were visualized using VMD 1.9 [19]. The host and guest structures that were obtained are shown in Fig. 1.

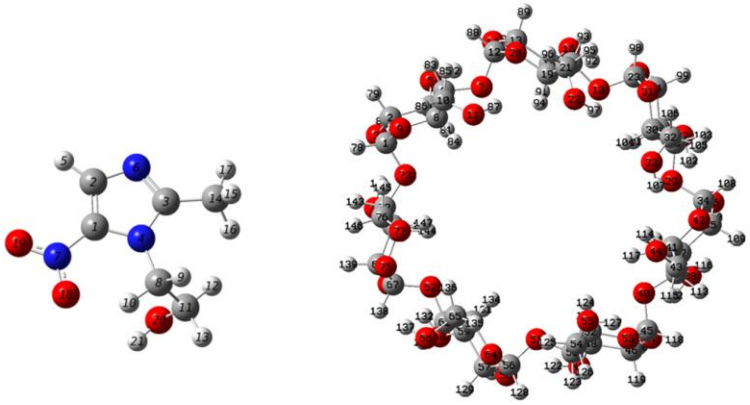

Figure. 1. Molecular structures and atom numbering of *β*-CD (host) and MNZ (guest).

To determine the most stable configuration of the MNZ@*β*-CD complex, where MNZ is enclosed within *β*-CD, we followed the method described in the literature [20]. A coordinate system was established with the glycosidic oxygen atoms of *β*-CD in the XY plane, with their center as the origin. The broad rim of the *β*-CD was aligned with the positive Z-axis. Two orientations were possible for the MNZ molecule to enter the *β*-CD: A, in which MNZ passes through the wide end of the *β*-CD, and B, in which MNZ enters the *β*-CD through the narrow end. The guest molecule (MNZ) position relative to the host (*β*-CD) was determined by aligning the bond between the N4 and C8 atoms of the MNZ molecule along the Z-axis, using the N4 atom as a reference point. The MNZ molecule was then systematically moved in both orientations along the Z-axis, with increments of 1 Å ranging from -7 Å to 7 Å. At each step, the MNZ molecule was rotated 3° around the Z-axis, completing a full 360° rotation (see Fig. 2). These steps enabled a thorough exploration of the potential energy surface of the MNZ@*β*-CD complex, resulting in the identification of its most stable configuration.

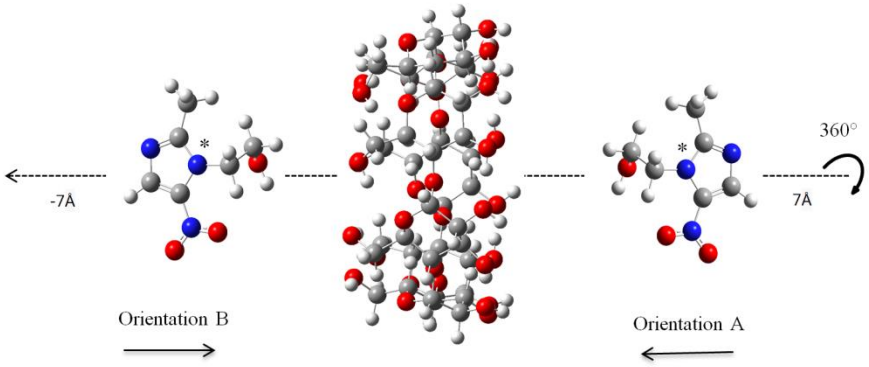

Figure. 2. Coordinate systems to describe inclusion processes of MNZ and β-CD.

Structures were fully optimized using the semi-empirical PM3 method. This method is known for its computational efficiency in calculating the cyclodextrin (CD) systems, making it a powerful tool for exploring the conformation of CD complexes [21–24]. Therefore, it was chosen to identify the minimum energy structures involved in the inclusion process of MNZ with *β*-CD, which were calculated by interaction energy [25] (Eq. (1)).

$$\Delta E_{int} = E_{MNZ@\beta-CD} - (E^{sp}_{MNZ} + E^{sp}_{\beta-CD}) \quad (1)$$

Where $E_{MNZ@\beta-CD}$ is the energy of the complex, E^{sp}_{MNZ} corresponds to the single point energy of the MNZ, and $E^{sp}_{\beta-CD}$ corresponds to *β*−CD in the optimized complexes. The two optimal structures were then re-optimized using the B3LYP/6-31G(d), PW6B95/6-31G(d), and PW6B95-D3/6-31G(d) functionals at a high computational level in both gas and aqueous phases. The interaction energy of the two complexes can be calculated using Eq. (1).

To define complexation energy, Eq. (2) was used [25, 26].

$$\Delta E_{comp} = E_{MNZ@\beta-CD} - (E_{MNZ} + E_{\beta-CD}) \quad (2)$$

Where $E_{MNZ@CD}$ is the energy of the complex, $E_{\beta-CD}$ and E_{MNZ} are the optimized energy of the free host and guest.

Finally, the energy required for deformation during the formation of the complex was calculated as the difference between the single-point energy of the fully optimized component and its energy in the complex [27] (Eqs. (3) and (4)):

$$E_{def}\,(\beta-CD) = E^{SP}_{\beta-CD} - E_{\beta-CD} \quad (3)$$

$$E_{def}\,(MNZ) = E^{SP}_{MNZ} - E_{MNZ} \quad (4)$$

3. Results and Discussion:

3.1 The energy of complexes:

The energy changes during the inclusion of MNZ into β-CD are represented as two distinct curves in Fig. 3.

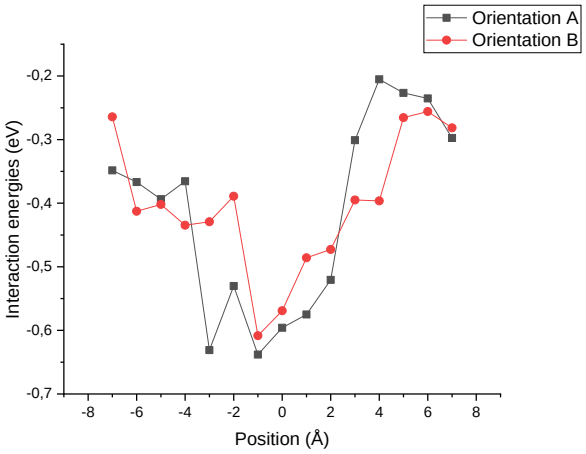

Figure. 3. Interaction energies of the inclusion of MNZ into *β*-CD optimized at different positions Z using (PM3 calculations).

The curves demonstrate that the minimum energy of the most stable structures is located at Z = -1 Å for both orientations A and B. The corresponding interaction energies are -0.638 eV for orientation A and -0.608 eV for orientation B. It is not possible to determine the preferred orientation due to the small energy difference of 0.030 eV. Therefore, both complexes were optimized using DFT theory. The results of the complexation, interaction, and deformation energies of orientations A and B in both gas and water phases are presented in Table 1. Based on these observations and comparisons, the following can be inferred:

The most favorable results for complexation and interaction energies were obtained using PW6B95-D3/6-31G(d). Based on the interaction energy, the gaseous phase is more stable. The same is true for the complexation energy, except in the case of B3LYP/6-31G(d), which favors the aqueous phase. The complexation energy indicates that orientation A is more favorable in PW6B95-D3/6-31G(d) with a difference of 4 kcal/mol and in B3LYP/6-31G(d) with a difference of 0.59 kcal/mol. Meanwhile, PW6B95/6-31G(d) revealed the opposite result, in which orientation B is favorable with a small difference of 0.33 kcal/mol. Regarding the interaction energy, orientation A is the most stable for PW6B95-D3/6-31G(d), PW6B95/6-31G(d), and B3LYP/6-31G(d), with relative energies of -49.9943 kcal/mol, -32.2120 kcal/mol, and -26.7878 kcal/mol, respectively.

Table 1 shows that *β*-CD exhibits higher deformation energy compared to the MNZ molecule in both orientations across all functionals. This underscores the significant impact of β-CD's flexibility in enhancing intermolecular interactions and ensuring the stability of the entire complex system. It is worth mentioning that the MNZ molecule in orientation B necessitates a higher amount of energy

for structural adaptation within the β-CD cavity. Notably, in both orientations, the complexation and interaction energies are negative, indicating the energetically favorable nature of incorporating MNZ into β-CD. This aligns with experimental enthalpy data, validating the favorable binding process [11].

	Gas		Water	
	Orientation A	**Orientation B**	**Orientation A**	**Orientation B**
B3LYP/6-31G (d)				
ΔE_{comp} (kcal/mol)	-10.9180	-10.3301	-11.1822	-8.6132
ΔE_{int} (kcal/mol)	-26.7878	-18.1645	-19.0192	-9.2991
$E_{def\ (\beta\text{-CD})}$ (kcal/mol)	16.8907	9.4133	-4.0386	-10.4047
$E_{def\ (MNZ)}$ (kcal/mol)	0.1086	-0.4493	0.1318	-0.6532
PW6B95\6-31G (d)				
ΔE_{comp} (kcal/mol)	-17.0356	-17.3651	-16.9722	-14.9491
ΔE_{int} (kcal/mol)	-32.2120	-27.7284	-24.4917	-18.1727
$E_{def\ (\beta\text{-CD})}$ (kcal/mol)	15.3075	10.9400	7.8382	3.9885
$E_{def\ (MNZ)}$ (kcal/mol)	-0.1311	-0.5767	-0.3188	-0.7650
PW6B953D\6-31G(d)				
ΔE_{comp} (kcal/mol)	-38.0572	-34.05693	-34.7640	-29.8851
ΔE_{int} (kcal/mol)	-49.9943	-44.2111	-41.7902	-34.9906
$E_{def\ (\beta\text{-CD})}$ (kcal/mol)	12.1411	10.7794	7.2992	5.7825
$E_{def\ (MNZ)}$ (kcal/mol)	-0.2039	-0.6375	-0.2730	-0.6771

Table. 1. Energies of MNZ@*β*-CD complexes in gas and aqua, calculated using high-level quantum chemistry methods.

The performance of the PW6B95 and PW6B95-D3 methods in predicting more stable geometric structures is better than that of the conventional B3LYP method, as demonstrated by the results obtained in both gas and aqueous phases. It can be concluded that PW6B95-D3 is the most accurate. The MNZ molecule is predominantly located within the β-CD cavity, regardless of its orientation, in both the gas and aqueous phases (see Fig. 4).

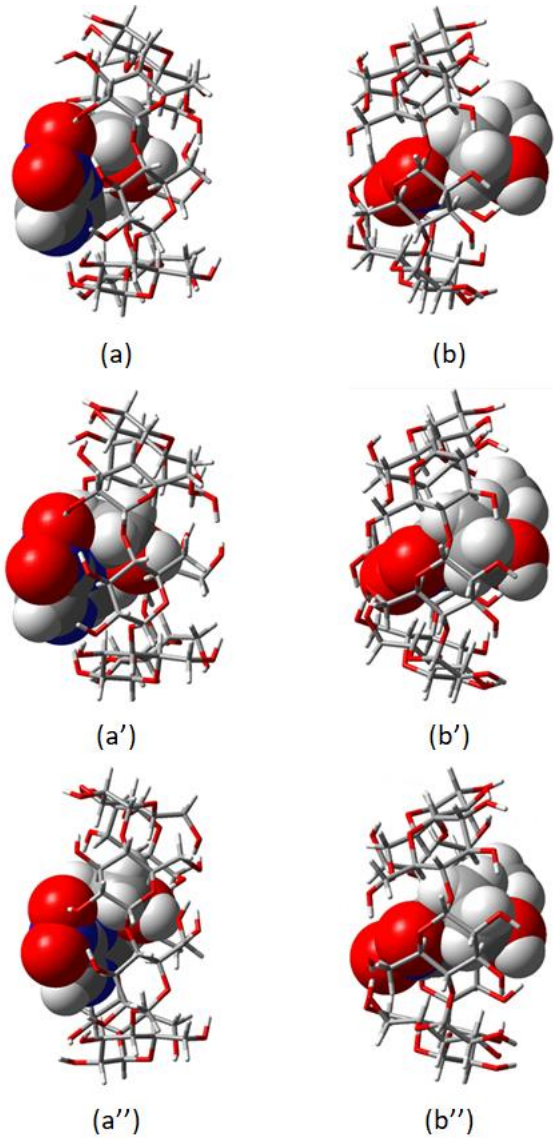

Figure. 4. Geometries of the most stable MNZ@β-CD complexes in aqueous phase, obtained with B3LYP/6-31G(d) (a, b) \ PW6B95/6-31G(d) (a′, b′) \ PW6B95-D3/6-31G(d) (a′′, b′′)

3.2 Frontier molecular orbital:

In the frontier molecular orbitals, also known as the HOMO (highest occupied molecular orbital) and LUMO (lowest unoccupied molecular orbital) [28], the HOMO acts as an electron donor, signifying its capability to donate electrons, while the LUMO functions as an electron acceptor, indicating its ability to accept electrons [29, 30]. Increased molecular stability and decreased reactivity can be inferred from a larger energy gap [31, 32]. The energy gap ($E_{HOMO-EELUMO}$) can be used to determine global chemical reactivity descriptors, such as electronic potential (μ), electronegativity (χ), chemical hardness (η), the global electrophilicity index (ω), electrophilicity-

based charge transfer (ECT) [33], and ΔN_{max}, which denotes the maximum electronic charge transfer [34]. The equations below are applied for the calculation:

$$\mu = (E_{HOMO} + E_{LUMO})/2 \quad (6)$$

$$\chi = -\mu = (E_{HOMO} + E_{LUMO})/2 \quad (7)$$

$$\eta = (E_{LUMO} - E_{HOMO})/2 \quad (8)$$

$$\omega = \mu\, 2\, /2\eta \quad (9)$$

$$\Delta N = \mu / \eta \quad (10)$$

$$ECT = (\Delta N_{max})\ host - (\Delta N_{max})\ guest \quad (11)$$

GAS

	Free MNZ	Free *β*-CD	A	B
PW6B95\6-31G(d) ; PW6B953D\6-31G(d)				
HOMO	-7.338 / -7.339	-7.074 / -7.112	-7.294 / -7.360	-7.344 / -7.343
LUMO	-2.092 / -2.095	1.289/ 1.333	-2.460 / -2.531	-2.685 / -2.730
Δ_{gap}	5.246 / 5.244	8.363 / 8.445	4.834 / 4.829	4.659 / 4.613
μ	-4.715 / -4.717	-2.893 / -2.890	-4.877 / -4.946	-5.015 / -5.037
η	2.623 / 2. 622	4.182 / 4.223	2.417 / 2.415	2.330 / 2.307
χ	4.715 / 4.717	2.893 / 2.890	4.877 / 4.946	5.0145 / 5.037
ω	4.238 / 2.243	1.001 / 0.989	4.920 / 5.065	5.400 / 5.500
ΔN	1.796 / 1.799	0.692 / 0.684	/	/
ECT	/	-1.104 / -1.115	/	/

WATER

	Free MNZ	Free *β*-CD	A	B
PW6B95\6-31G(d) ; PW6B953D\6-31G(d)				
HOMO	-7.258 / -7.259	-7.276 / -7.352	-7.332 / -7.378	-7.364 / -7.395
LUMO	-2.180 / -2.182	1.614 / 1.680	-2.571 / -2.561	-2.626 / -2.710
Δ_{gap}	5.078 / 5.077	8.890 / 9.032	4.761 / 4.817	4.738 / 4.685
μ	-4.719 / -4.721	-2.831 / -2.836	-4.952 / -4.970	-4.995 / -5.053
η	2.539 / 2.538	4.445 / 4.516	2.381 / 2. 409	2.369 / 2.343
χ	4.719 / 4.721	2.831 / 2.836	4.952 / 4.970	4.995 / 5.053
ω	4.385 / 4.391	0.902 / 0.890	5.150 / 5.127	5.266 / 5.450
ΔN	1.859 / 1.860	0.637 / 0.628	/	/
ECT	/	-1.222 / -1.232	/	/

Table. 2. The global reactivity indexes of β-CD, MNZ and their inclusion complexes in PW6B95\6-31G(d), B3LYP\6-31G(d) and PW6B95-D3\6-31G(d) in aqueous and gaseous phases.

Table 2 summarizes the global reactivity indices obtained using PW6B95/6-31G(d) and PW6B953D/6-31G(d) in both gas and water. It shows that in both aqueous and gaseous phases, the HOMO-LUMO gap for orientation A is higher than that of Orientation B, supporting the stability of orientation A. The negative chemical potential is a determinant of the stability and the spontaneous formation of a complex between MNZ and the *β*-CD in both orientations, either in gas or water. Additionally, charge transfer occurs from the host *β*-CD to the guest molecule MNZ, which has a lower electronic chemical potential. The global hardness (η) of the complexes decreases while the electronegativity parameter increases upon entering the cavity of the β-CD. Proportional values of (η) and HOMO-LUMO gap suggest that the complex in orientation A in gas is the most stable, with the hardest global hardness of 2.417/2.415 eV and the largest HOMO-LUMO gap of 4.834/4.829 eV, by PW6B95/6-31G(d) and PW6B953D/6-31G(d) respectively. Orientation B has a significantly higher calculated electrophilicity than orientation A, making it the most electrophilic complex. To verify the direction of charge transfer, we employed electrophilicity-based charge transfer ECT. A negative ECT value indicates that the charge is transferred from β-CD to MNZ. The results also show that the highest occupied molecular orbital (HOMO) is mainly located on the host (β-CD), while the lowest unoccupied molecular orbital (LUMO) is situated on the guest molecule (MNZ). (Fig. 5) depicts reciprocal interactions between β-CD and MNZ.

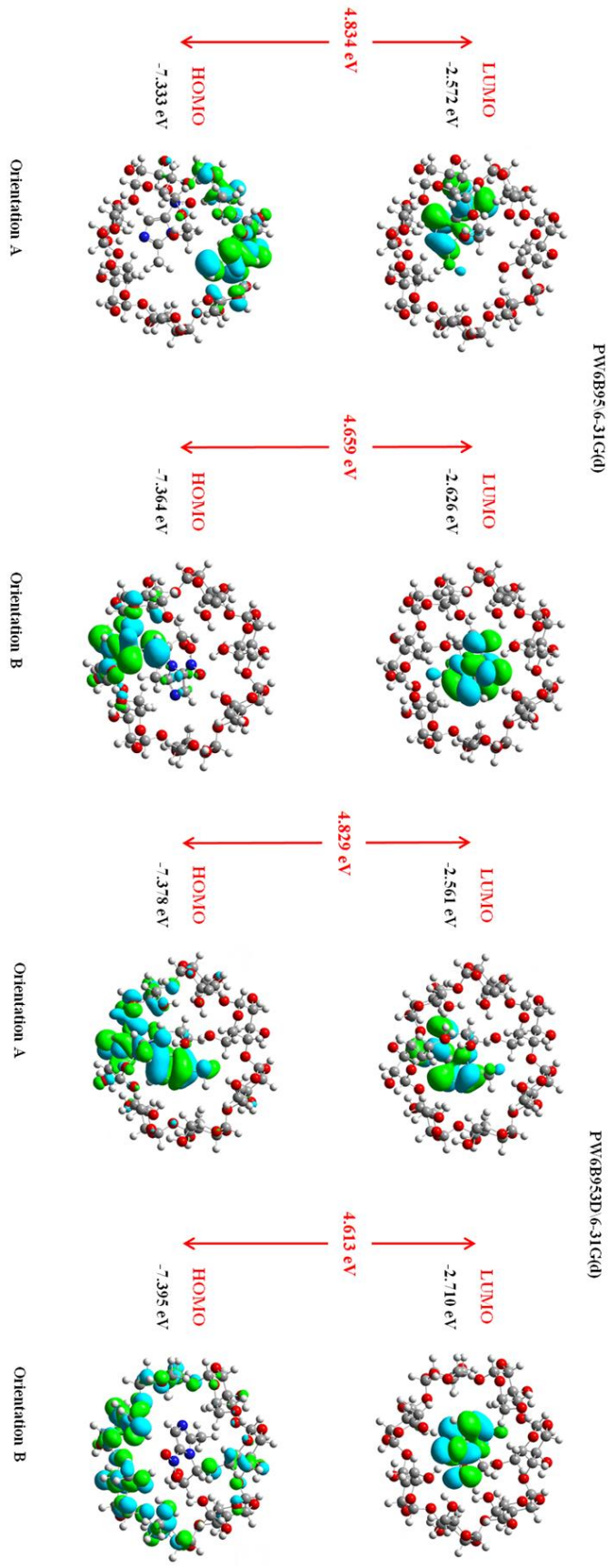

Figure. 5. The FMOs of MNZ@β-CD obtained by PW6B95\6-31G (d); PW6B953D\6-31G (d).

3. 3. ^{1}H NMR analysis:

Proton NMR spectroscopy is employed to provide additional evidence for the encapsulation of MNZ within the *β*-CD cavity while also providing insight into the geometry and positioning of the guest molecule within. DFT calculations were carried out to determine the preferred mode of complexation (orientation A or B) by comparison with experimental ^{1}H NMR data, using the GIAO method to evaluate chemical shifts relative to TMS [35, 36]. The chemical shifts for free MNZ were assessed using the B3LYP/6-31G(d) level of calculation, with single-point calculations on PW6B95-D3/6-31G(d) optimized geometries. This method is adequate for calculating NMR spectra for organic molecules. The obtained ^{1}H NMR chemical shifts of MNZ before and after complexation are documented in Table 3 and Fig. 6.

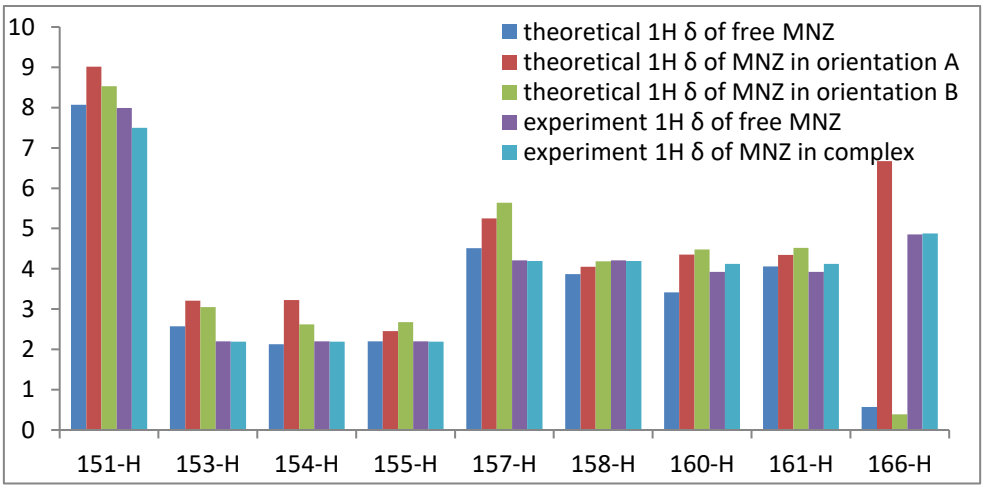

Figure. 6. Calculated (GIAO method at B3LYP/6-31G (d)) and experimental ^{1}H NMR chemical shifts (ppm) of MNZ before and after complexation.

	Calculated					Experimental [10]	
Protons	δ Free MNZ	δ MNZ in orientation A	Δδ	δ MNZ in orientation B	Δδ	δ Free MNZ	δ MNZ in complex
151-H	8,07	9,02	0.95	8,53	0.46	7,99	7.50
153-H	2,57	3,21	0.64	3,05	0.48	2,20	2.19
154-H	2,13	3,22	1.09	2,62	0.49	2,20	2.19
155-H	2,20	2,45	0.25	2,67	0.47	2,20	2.19
157-H	4,51	5,25	0.74	5,64	1.13	4,22	4.20
158-H	3,87	4,05	0.18	4,18	0.31	4,22	4.20
160-H	3,41	4,35	0.94	4,48	1.07	3,92	4.12
161-H	4,06	4,34	0.28	4,52	0.46	3,92	4.12

Table. 3. Experimental and calculated chemical shifts of free MNZ protons and inclusion complexes MNZ/*β*-CD using the GIAO approach, B3LYP/6-31G(d).

Furthermore, it is widely accepted that alterations in chemical shifts result from hydrogen bond interactions. The computed NMR data provides detailed information on chemical shifts, enabling the precise identification of individual hydrogen atoms.

Table 3 shows significant differences in chemical shifts before and after complexation, particularly for protons H157 of MNZ in orientation A, H154 in orientation B, and H160 in orientation B, with differences of 1.09/1.13/1.07 ppm, respectively. These shifts are attributed to the guest molecule MNZ within the *β*-CD cavity, indicating the formation of the inclusion complex. The largest difference between the theoretical and experimental chemical shifts is observed in protons H151 with a difference of 1.52 ppm and H157 with a difference of 1.44 ppm. This aligns with the experimental results [10], which confirm the inclusion of the guest molecule into the host cavity.

3. 4. Natural bond orbital analysis:

In the natural bond analysis method, the second-order stabilization energy, denoted by $E^{(2)}$, is a quantitative assessment of the stabilizing effect resulting from electronic delocalization between occupied Lewis-type natural bond orbitals NBOs acting as donors and formally unoccupied non-Lewis NBOs acting as acceptors [37, 38]. These interactions drive the delocalization of electrons from bonding (BD) or nonbonding (LP) orbitals to antibonding (BD*) orbitals [39]. The $E^{(2)}$ value infers the strength of electron donation and the extent of conjugation in a system. A larger $E^{(2)}$ value indicates stronger interactions between electron donors and acceptors [40]. Table 4 summarizes the significant interactions and their respective $E^{(2)}$ energies for the two orientations, calculated using the PW5B95/6-31G(d) and PW5B95-D3/6-31G(d) levels of theory.

In orientation A, the optimal value of $E^{(2)}$ was determined by PW6B95-D3/6-31G(d), which corresponds to the transition LP(2) (O11) to σ*(1) (O165-H166) (24.06 kcal/mol). However, PW6B95/6-31G(d) demonstrates superior performance in providing accurate $E^{(2)}$ values across the other transitions. Meanwhile, in orientation B, PW6B95-D3/6-31G(d) performed better in predicting $E^{(2)}$ values for all transitions, with the optimal transition being from LP(2) (O168) to σ*(1) (O33-H107) (10.60 kcal/mol). As a donor molecule, MNZ forms a significant intermolecular hydrogen bond in orientation A. This delocalization involves the interaction between the lone pair (LP)(2) of O167 and the antibonding orbital (σ*)(1) of O14-H90. The stabilization energy is 9.14 kcal/mol obtained with PW6B95/6-31G PW6B95/6-31G(d), 6.98 kcal/mol obtained with PW6B95-D3/6-31G (d). In orientation B, there is an interaction between the lone pair (LP)(2) of O168 and

the antibonding orbital (σ*)(1) of O33-H107, resulting in stabilization energy of 9.64 kcal/mol given by PW6B95/6-31G (d) 10.60 kcal/mol given by PW6B95-D3/6-31G (d). When MNZ acts as an acceptor molecule, orientation A displays hydrogen bonds, mostly noticed between the lone pairs (LP)(2) and (1) of O11 interacting with the antibonding orbital (σ*)(1) of the O165-H166 bond. Additionally, in orientation B, there are weaker interactions observed between (LP)(2) of O77 and the antibonding orbital (σ*)(1) of C156-H157 with a stabilization energy of 0.87/1.72 kcal/mol, as well as between (σ)(1) of O11-H84 and the antibonding orbital (σ*)(1) of O156-H157 with an $E^{(2)}$ of 0.58/1.07 kcal/mol, respectively.

Orbital donor	Orbital acceptor	$E^{(2)}$ (kcal mol^{-1}) PW6B95/6-31G(d)	$E^{(2)}$ (kcal mol^{-1}) PW6B95-D3/6-31G(d)
Orientation A			
β-CD → MNZ			
LP(2) (O11)	σ*(1) (O165-H166)	8.94	24.06
LP(1) (O11)	σ*(1) (O165-H166)	5.94	1.61
LP(1) (O7)	σ*(1) (O165-H161)	1.59	1.87
MNZ → β-CD			
LP(2) (O167)	σ*(1) (O14-H90)	9.14	6.98
LP(1) (O167)	σ*(1) (O14-H90)	4.57	3.05
Orientation B			
β-CD → MNZ			
LP(2) (O77)	σ*(1) (C156-H157)	0.87	1.72
σ (1) (O11-H84)	σ*(1) (O156-H157)	0.58	1.07
MNZ → β-CD			
LP(2) (O168)	σ*(1) (O33-H107)	9.64	10.60
LP(1) (O168)	σ*(1) (O33-H107)	3.10	4.69
LP(1) (O168)	σ*(1) (O44-H117)	2.29	4.90

Table. 4. The most significant donor-acceptor interactions and their corresponding $E^{(2)}$ energies obtained using PW6B95/6-31G(d) and PW6B95-D3/6-31G(d) in the aqueous phase.

3. 5. Quantum atom in molecule analysis:

The objective of this study was to perform a Quantum Theory of Atoms in Molecules [41] (QTAIM) analysis to investigate the nature of host-guest interactions and categorize bonding interactions based on quantum mechanical parameters [42]. The topological parameters that determine the properties of Bond Critical Points (BCPs) are as follows: The electron density (ρ) and its Laplacian of the electron density ($\nabla^2\rho$) are the principal topological parameters used to define the properties of BCPs [43,44]. Additionally, the kinetic energy densities G(r), the potential V(r), the

local electron energy densities H(r) (with H(r) = G(r) + V(r)), the ratio of the local gradient - G(R)/V(R), the bond energy E (E_{bond} = V(r)/2)[45] and the eigenvalues (λ_i) of the Hessian (a.u.) are also included in this analysis. Furthermore, the ellipticity index ε, defined as (λ_1/λ_2 - 1), is considered [46]. The bond critical point (BCP) represents a specific point on the bond path where ($\nabla\rho = 0$) [47], indicating the presence of a chemical bond or interaction between two nuclei. Bader's theory [48] states that covalent (polar) bonds can be differentiated from interactions between closed-shell systems (ionic interactions, vdW interactions, or H-bonds) when $\nabla^2\rho(r) < 0$, and both the values of $\nabla^2\rho(r)$ and ρ are large: this indicates a covalent (polar) bond. When $\nabla^2\rho(r) > 0$ and the values of $\nabla^2\rho(r)$ and ρ are low, this shows interactions between closed-shell systems. Koch and Popelier [49] proposed three criteria to confirm the properties of the bonds, especially hydrogen bonds: (i) The confirmation of the presence of a hydrogen bond is indicated by the existence of a BCP between the "H" of the donor group and the acceptor group. (ii) The range of values for forming a H-bond is 0.002-0.040 a.u. for ρ. (iii) The Laplacian $\nabla^2\rho(r)$ must be positive and within $0.024 < \nabla^2\rho(r) < 0.139$ a.u. The correlation between $\rho_{(BCP)}$ and the $E_{H\text{-}b}$ is noteworthy. In addition to the aforementioned criterion, Nakanishi et al. [50, 51] presented a further criterion to categorize and differentiate between H-bonds and van der Waals interactions, which depend on the values of ρ, $\nabla^2\rho$, and H(r) as follows: (i) H-bond: 0.01 a.u < ρ(r) < 0.04 a.u, 0.06 a.u < $\nabla^2\rho(r)$ < 0.12 a.u, and -0.01 a.u < H(r) < 0.003 a.u. (ii) vdW interaction: 0.00 a.u < ρ(r) < 0.01 a.u, 0.00 a.u < $\nabla^2\rho(r)$ < 0.05 a.u, and 0.00 a.u < H(r) < 0.003 a.u.
The strength of H-bonds can be classified according to Rozas et al. [45, 52]. as follows: (i) $\nabla^2\rho(r) < 0$, H(r) < 0: strong covalent H-bond. (ii) $\nabla^2\rho(r) > 0$, H(r) < 0: medium H-bond. (iii) $\nabla^2\rho(r) > 0$, H(r) > 0: weak H-bond.

This study presents a comparative analysis of the performance of PW6B95/6-31G(d) and PW6B95-D3/6-31G(d) levels of theory in predicting the topological parameters of our MNZ@β-CD inclusion complexes for the two orientations in the aqueous phase. All of the characteristics of BCPs designated as H---X (X: H, C, O, N) are presented in Table 5.S. All BCPs and bond paths of MNZ@β-CD in water, determined by PW6B95/6-31G(d) and PW6B95-D3/6-31G(d), are presented in Fig. 7.

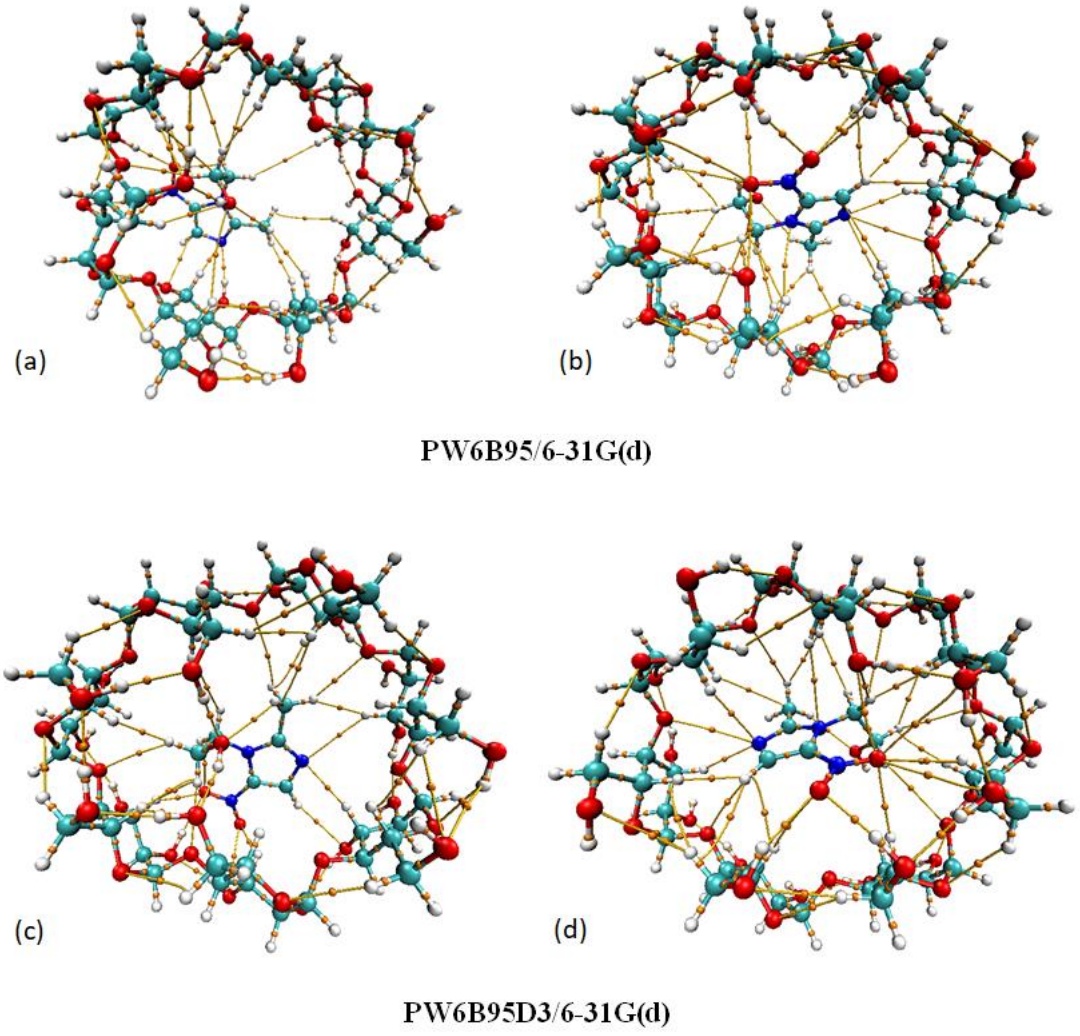

Figure. 7. Molecular topography analysis of MNZ@*β*-CD complex (orientation A (a, c) and orientation B (b, d)) obtained using PW6B95/6-31G(d) and PW6B95-D3/6-31G(d) in the aqueous phase.

From Table 5. S, ρ(r) with the corresponding Laplacian $\nabla^2\rho(r)$ in Orientation A ranged as follows: 0.0017 a.u ≤ ρ(r) ≤ 0.0291 a.u and 0.0054 a.u ≤ $\nabla^2\rho(r)$ ≤ 0.0913 a.u for the PW6B95/6-31G(d) method. For the PW6B95-D3/6-31G(d) method, the values were 0.003 a.u. ≤ ρ(r) ≤ 0.0345 a.u. and 0.0105 a.u. ≤ $\nabla^2\rho(r)$ ≤ 0.101 a.u. In Orientation B, the values were 0.0031 a.u ≤ ρ(r) ≤ 0.0267 a.u and 0.013 a.u ≤ $\nabla^2\rho(r)$ ≤ 0.082 a.u using the PW6B95/6-31G(d) method. The PW6B95-D3/6-31G(d) method yielded results of 0.0022 a.u. ≤ ρ(r) ≤ 0.0312 a.u. and 0.0077 a.u. ≤ $\nabla^2\rho(r)$ ≤ 0.098 a.u. Positive values of $\nabla^2\rho(r)$ in all BCPs indicate the absence of covalent bonds in host-guest interactions.

Most of the values of the electron density (ρ) and its Laplacian of the electron density ($\nabla^2\rho$) align with the Nakanishi et al. criterion for H-bonds, while others fall within the commonly accepted

limits for van der Waals interactions. This confirms that the majority of the interactions and bonds between MNZ and β-CD are hydrogen bonds.

By considering the values of the local electron energy densities H(r), we can apply the classification proposed by Rozas et al. to the interactions between MNZ and *β*-CD. As mentioned earlier, all Laplacian electron density ($\nabla^2\rho$) values are completely positive. Furthermore, it is notable that the majority of the H(r) values are positive, with the ratio of $-G(r)/V(r) > 1$, indicating the presence of the weak H-bonds. However, some negative values of H(r) are observed, where the ratio of $-G(r)/V(r)$ is < 1, signifying medium hydrogen bonds that contribute to stabilizing our inclusion complexes MNZ@β-CD, this is pertinent to the following BCPs: H140···N163 (H(r) = -0.0007 a.u.), H166···O11 (H(r) = -0.0013 a.u.), and H90···O167 (H(r) = -0.0010 a.u.) in Orientation A given by the PW6B95/6-31G(d) method. Two medium hydrogen bonds appeared in the case of PW6B95-D3/6-31G(d): H117···O165 beside H90···O167, where H(r) = -0.0023 and -0.0009 a.u., respectively. In orientation B, both PW6B95/6-31G(d) and PW6B95-D3/6-31G(d) exhibited the same medium H-bond between H107 and O168, where the local electron energy densities were H(r) = -0.0011 and -0.0012 a.u., respectively. It is important to highlight that these specified bonds and their H(r) values correspond to the lowest values of path distances (d(Å)) related to the BCPs and the highest values of electron density ρ(r) and Laplacian $\nabla^2\rho(r)$.

Moreover, by analyzing the bond energy (E) values, it is clear that the lowest bond energy values are identical to those mentioned above. This supports the conclusion that these bonds are the most important and strongest intermolecular interactions in all complexes. These same interactions have previously appeared in the NBO analysis, which showed the strongest interactions between electron donors and acceptors (optimal $E^{(2)}$ values). This confirms the findings of that study, providing further understanding of the nature and strength of the intermolecular interactions.

The results of hydrogen bond energies $E_{H...X}$ for MNZ@β-CD in orientation A showed values ranging from -0.866 to -33.311 kcal/mol with the PW6B95/6-31G(d) method and from -1.496 to -38.850 kcal/mol with the PW6B95-D3/6-31G(d) method. Additionally, $E_{H...X}$ values in orientation B ranged from -1.943 to -29.860 kcal/mol and -1.142 to -35.359 kcal/mol using the PW6B95/6-31G(d) and PW6B95-D3/6-31G(d) methods, respectively. The calculated bond energy results in the table also indicated that the highest energy values corresponded to H-type interactions. Furthermore, there were other H···O interactions with high energy due to the large distance values between the atoms involved. The methods PW6B95/6-31G(d) and PW6B95-D3/6-31G(d) produced

structures with a high degree of similarity in the interacting atoms in both the orientation A and orientation B complexes.

The observed differences can be attributed to the deformation occurring in β-CD and MNZ structures during the complexation, depending on the DFT method used. The delocalization of electrons by the corresponding atoms is indicated by the low values of the ellipticity index ε.

λ_1, λ_2, and λ_3 represent the eigenvalues of the Hessian of the electron density, where $\lambda_1 < \lambda_2 < \lambda_3$. Furthermore, it can be seen that as the H···O distances increase ($\lambda_1 + \lambda_2$), the value of ($\lambda_1 + \lambda_2$) and (λ_3) decrease.

3. 6. Non-covalent interactions-reduced density gradient analysis:

The NCI analysis is a recently used approach to investigate weak interactions from the AIM analysis [53], including hydrogen bonds, van der Waals interactions, and repulsive steric interactions [54]. The colors used in the NCI-RDG isosurfaces have specific meanings: blue indicates stabilizing hydrogen bonding, green represents van der Waals interactions, and red signifies destabilizing steric interactions [55]. However, in the NCI-RDG scatterplots, the type of interaction is indicated by the sign (λ_2) ρ: attractive interactions are indicated by sign (λ_2) $\rho < 0$, repulsive interactions by sign (λ_2) $\rho > 0$, and weak van der Waals interactions by sign (λ_2) $\rho \approx 0$ [56].

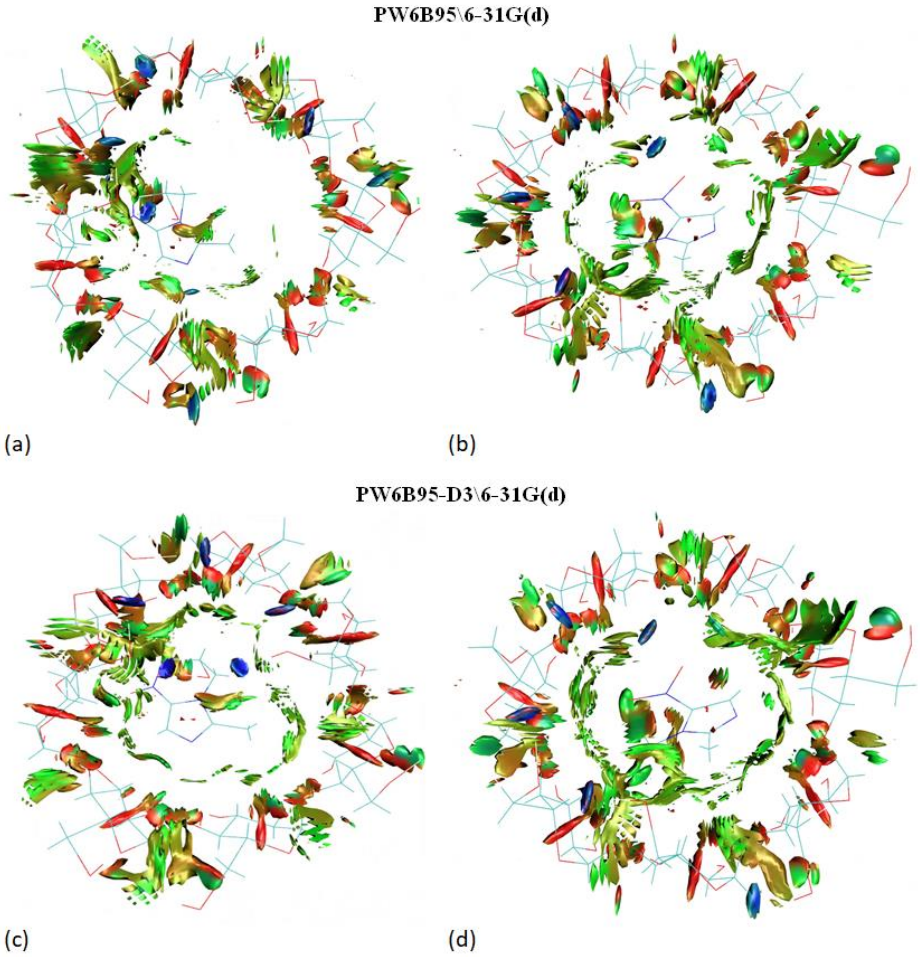

Figure. 8. NCI-RDG isosurfaces of MNZ@β-CD (orientation A (a, c) and orientation B (b, d)) obtained using PW6B95/6-31G(d) and PW6B95-D3/6-31G(d) in the aqueous phase.

In Figs. 8 and 9, disk-shaped isosurfaces encircle the MNZ molecule, and the RDG scatter map exhibits prominent green solid spikes, indicating the presence of non-covalent interactions between MNZ and *β*-CD mediated by van der Waals forces. Fig. 7 shows the 3D visualization of the NCI interaction, where blue and blue-green disk-shaped regions indicate the presence of strong and medium hydrogen bonds. In orientation A, when comparing the RDG scatter points on the map in Fig. 8 for both methods, we can see a higher concentration of blue scatter points in the region of the negative scale after the value of -0.03 a.u. in PW6B95/6-31G(d) compared to PW6B95-D3/6-31G(d); in other words, there are more strong H-bonds in PW6B95/6-31G(d). Additionally, the 3D spatial NCI isosurface diagram illustrates the spatial distribution of the blue patches. The visualization in PW6B95/6-31G(d) shows blue disk-shaped regions that indicate the presence of strong H-bonds towards O44, O31, and O11. Bluish-green disk-shaped patches indicate medium H-bonds towards O22, N163, and O77. In PW6B95-D3/6-31G(d), five blue disk shapes are observed, indicating the presence of five strong H-bonds: O165, O44, O33, O22, and O11.

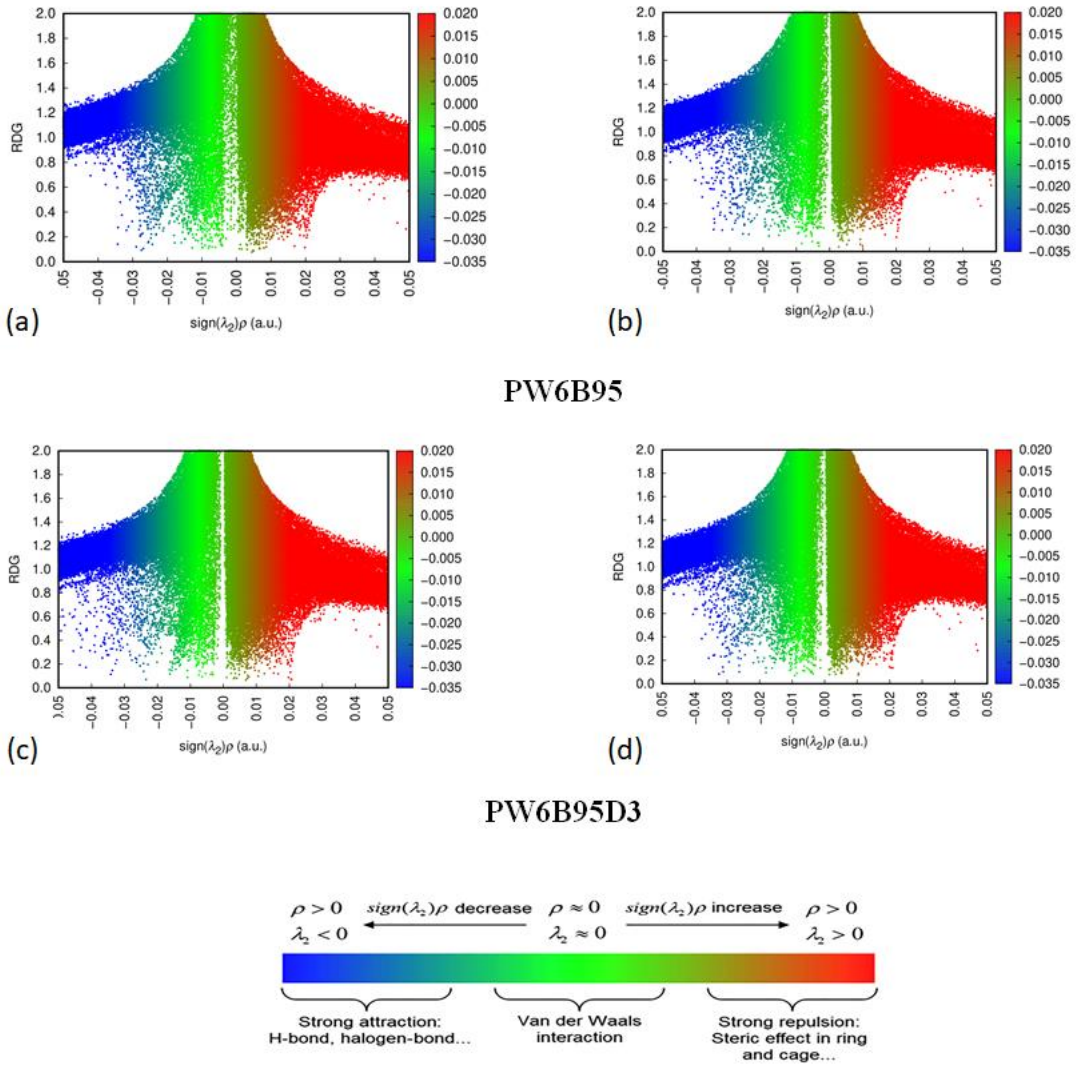

Figure. 9. NCI-RDG scatter plots of MNZ@β-CD (orientation A (a, c) and orientation B (b, d)) obtained using PW6B95/6-31G(d) and PW6B95-D3/6-31G(d) in the aqueous phase.

However, in orientation B, both methods PW6B95/6-31G(d) and PW6B95-D3/6-31G(d) exhibit great similarity in the positions of these blue spots. Specifically, O33···H97, O11···H147, and O22···H87 appear as blue spots corresponding to strong H-bonds, while O168···H107 and O75···H137 appear as bluish-green spots corresponding to medium H-bonds. The RDG scatter map confirms these observations. The red areas observed demonstrate steric repulsion and are localized mostly in the middle of the heterocycle rings and near the oxygens of the carbonyl groups of *β*-CD.

3. 7. IGM analysis:

In contrast to NCI analysis, the Independent Gradient Model (IGM) can separately quantify inter- and intramolecular interactions [57], developed by Lefebvre et al. [58, 59], it is constructed through the visualized noncovalent interplay of pieces. The IGM function δg^{inter} describes the intermolecular

interactions, while δg^{intra} describes the intramolecular interactions. Additionally, the sign (λ_2) ρ function is used, where λ_2 represents the second largest eigenvalue of the Hessian matrix of electron density ρ.

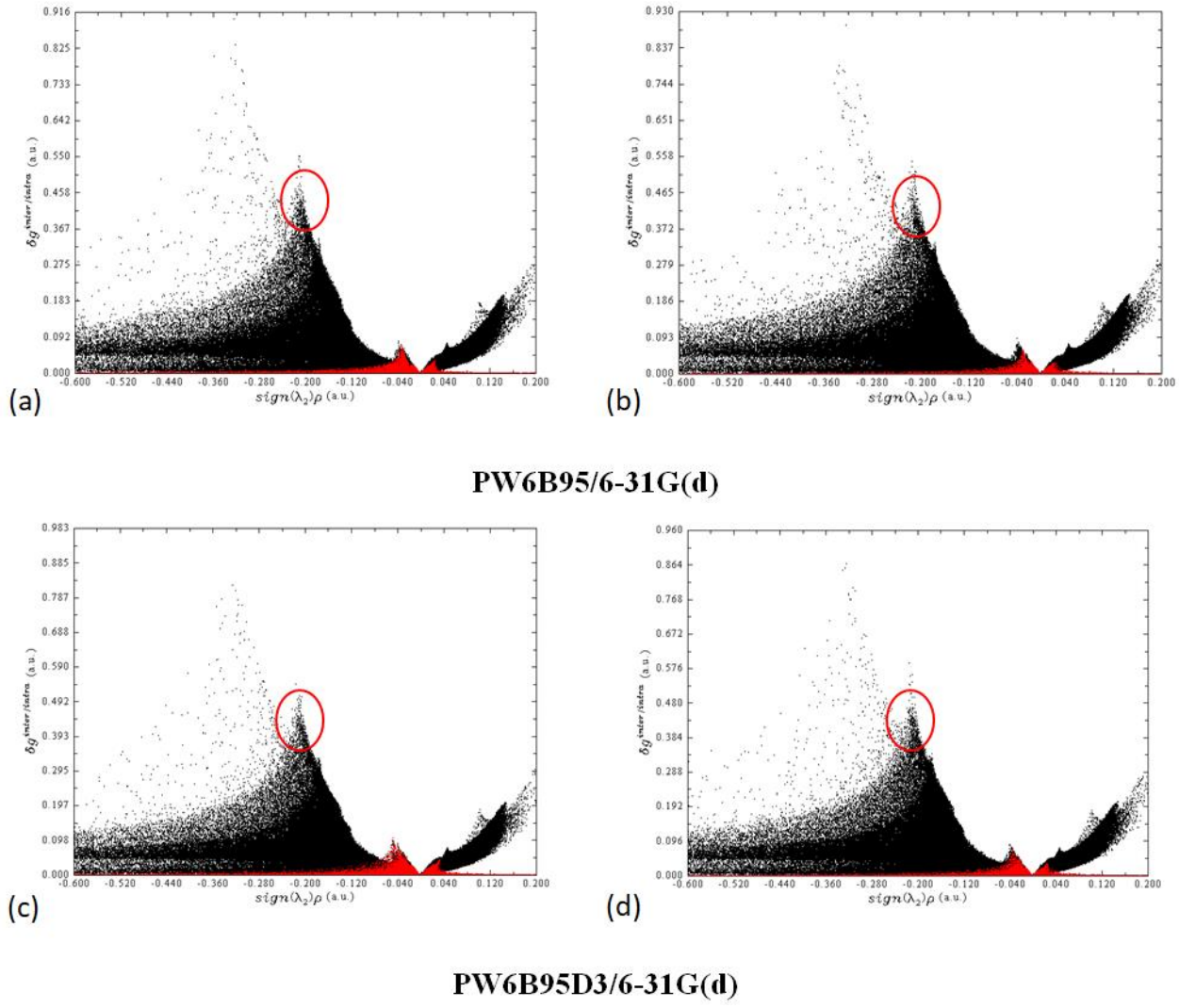

Figure. 10. IGM Scatter plots of MNZ@β-CD (orientation A (a, c) and orientation B (b, d)) obtained using PW6B95/6-31G (d) and PW6B95-D3/6-31G (d) in the aqueous phase.

(Fig. 10) illustrates the scatter graph of ($\delta g^{inter/intra}$) and electron density curvature (sign (λ_2)ρ) in all MNZ@*β*-CD complexes. The red points represent δg^{inter}, while the black points represent δg^{intra}. Upon analyzing the scatter plots in Fig. 10, it can be concluded that the strongest intrafragment covalent-bonding interaction in all the complexes corresponds to the significant peak of intramolecular interactions (surrounded by the red circle) around (sign ($\lambda 2$) ρ) ≈ 0.430 (a.u.) and (δg^{intra}) ≈ -0.220 (a.u.).

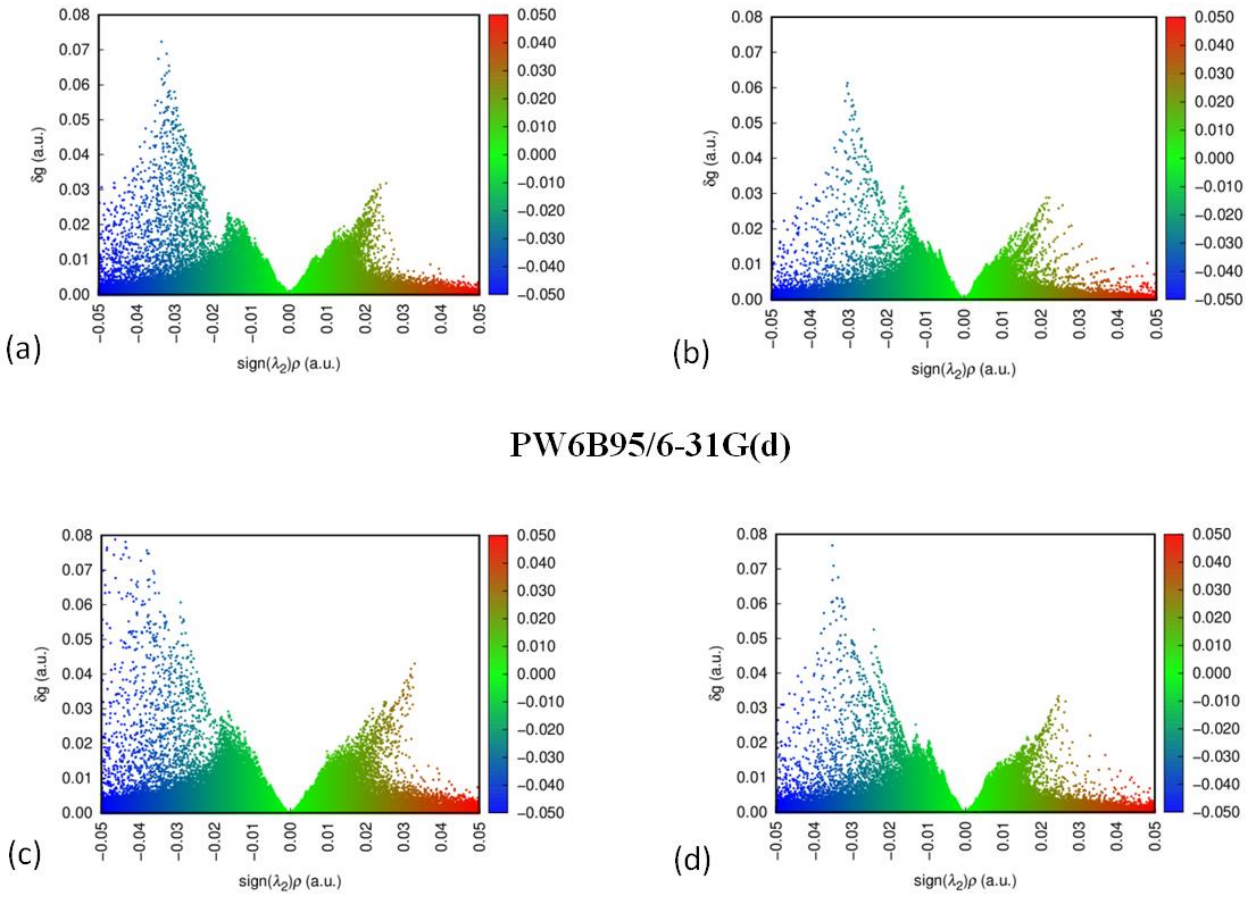

Figure. 11. IGM-RDG scatter plots of MNZ@β-CD (orientation A (a, c) and orientation B (b, d)) obtained using PW6B95/6-31G(d) and PW6B95-D3/6-31G(d) in the aqueous phase.

To gain a better understanding of the information that can be extracted from δg^{inter}, consider the RDG scattering plots shown in Fig. 11. The high δg^{inter} values correspond to the blue and green dense peaks at the negative field, indicating that the H-bond and van der Waals interactions are stronger and the binding system of the inclusion complexes is stable. Since the H-bond interactions are the strongest, and based on the density and δg^{inter} values of the blue scatter points, it can be concluded that the complexes optimized with the PW6B95-D3/6-31G(d) method are more stable, with orientation A being the most stable.

The IGM isosurfaces in Fig. 12 confirm the information above and show the location and type of each interaction. The green areas represent the van der Waals interaction, while the blue disks represent the H-bond interaction. In accordance with the developer's tutorial [60], the atoms were colored based on their atom δg indices; the degree of redness of atoms is proportional to the atom δg index, as indicated in [61], which enables a clearer understanding of the atoms involved in the

interactions (see Fig. 12). The majority of MNZ's atoms and some of β-CD's atoms contributed to the intermolecular interactions, while interactions from white-colored atoms can be ignored. It is observed that all atoms of β-CD that interact with MNZ are distributed around it. However, in the case of complex (a) (orientation A optimized with PW6B95/6-31G(d)), all interactions are concentrated on one side of the cavity due to a geometric change that occurred during optimization. Furthermore, the observation of the cyclodextrin atoms involved allows us to confirm the significant role played by the primary hydroxyl rim of β-cyclodextrin in the complexation process.

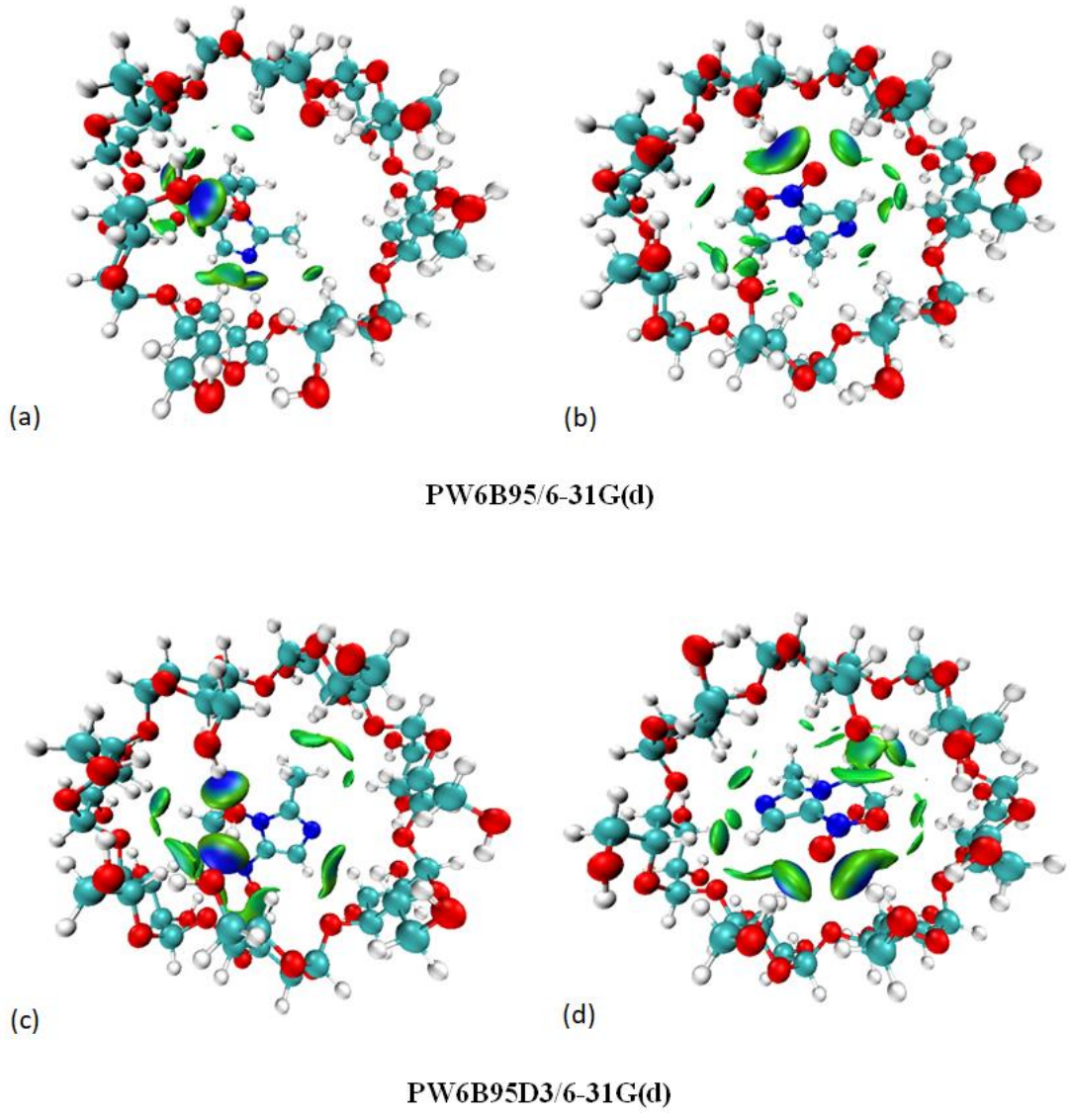

Figure. 12. IGM-RDG isosurfaces of MNZ@β-CD (orientation A (a, c) and orientation B (b, d)) obtained using PW6B95/6-31G (d) and PW6B95-D3/6-31G (d) in the aqueous phase.

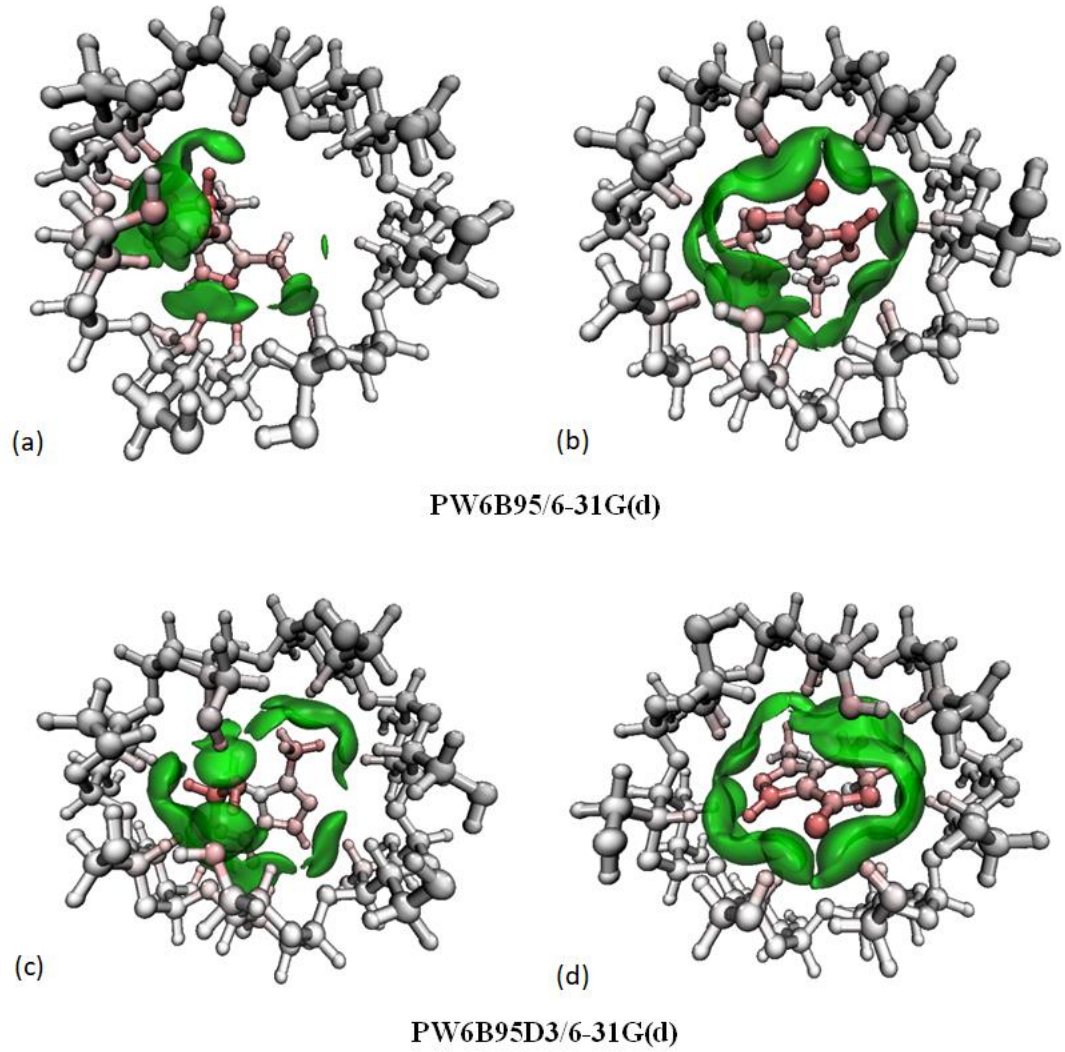

Figure. 12. IGM isosurfaces and atom δ g indices of MNZ@β-(orientation A (a, c) and orientation B (b, d)) obtained using PW6B95/6-31G (d) and PW6B95-D3/6-31G (d) in the aqueous phase.

4. CONCLUSION

This paper reports a computational study on the interactions in a complex of 1:1 stoichiometry (β-cyclodextrin and metronidazole). A high level of theory has been used to compare two of the most recently developed methods: the basic functional PW6B95 and its dispersion correction (D3) PW6B95-D3, in addition to the conventional method B3LYP.

Metronidazole can spontaneously enter the cavity of β-cyclodextrin in two orientations in both gaseous and aqueous phases. Orientation A is generally the most favorable, except for the case of the PW6B95 method in the gaseous phase. The PW6B95 and PW6B95-D3 functionals are more accurate than B3LYP, with PW6B95-D3 being the most precise.

GIAO NMR calculations indicate that PW6B96-D3 predicts well compared to the experimental results.

The distribution charge changes during the inclusion process, according to NBO analysis.

Interpreting the results of QTAIM analysis confirms the vital role of weak H-bonds and vdW interactions in stabilizing the inclusion complex.

NCI-RDG and IGM analyses are in good agreement with QTAIM results. NCI analysis enables us to identify and confirm hydrogen bonds, vdW, and steric and steric repulsion involved in stabilizing our inclusion complexes. In contrast, IGM provides a quantitative perspective on these inter- and intra-molecular interactions, illustrating the specific atoms involved.

5. REFERENCES

[1] Qiu, N., Zhao, X., Liu, Q., Shen, B., Liu, J., Li, X., & An, L. (2019). Inclusion complex of emodin with hydroxypropyl-β-cyclodextrin: Preparation, physicochemical and biological properties. Journal of Molecular Liquids, 289, 111151, doi: 10.1016/j.molliq.2019.111151.

[2] Tang, P., Li, S., Wang, L., Yang, H., Yan, J., & Li, H. (2015). Inclusion complexes of chlorzoxazone with β-and hydroxypropyl-β-cyclodextrin: characterization, dissolution, and cytotoxicity. Carbohydrate polymers, 131, 297-305, doi: 10.1016/j.carbpol.2015.05.055.

[3] Sharma, N., & Baldi, A. (2016). Exploring versatile applications of cyclodextrins: an overview. Drug delivery, 23(3), 729-747, doi: 10.3109/10717544.2014.938839.

[4] Perioli, L., Ambrogi, V., Rubini, D., Giovagnoli, S., Ricci, M., Blasi, P., & Rossi, C. (2004). Novel mucoadhesive buccal formulation containing metronidazole for the treatment of periodontal disease. Journal of controlled release, 95(3), 521-533, doi: 10.1016/j.jconrel.2003.12.018.

[5] Flemmig, T. F., Milian, E., Kopp, C., Karch, H., & Klaiber, B. (1998). Differential effects of systemic metronidazole and amoxicillin on Actinobacillus actinomycetemcomitans and Porphyromonas gingivalis in intraoral habitats. Journal of clinical periodontology, 25(1), 1-10, doi: 10.1111/j.1600-051X.1998.tb02356.x.

[6] Freeman, C. D., Klutman, N. E., & Lamp, K. C. (1997). Metronidazole: a therapeutic review and update. Drugs, 54, 679-708, doi: 10.2165/00003495-199754050-00003.

[7] De Oliveira, H. P., Tavares, G. F., Nogueiras, C., & Rieumont, J. (2009). Physico-chemical analysis of metronidazole encapsulation processes in Eudragit copolymers and their blending with amphiphilic block copolymers. International journal of pharmaceutics, 380(1-2), 55-61, doi: 10.1016/j.ijpharm.2009.06.028.

[8] Prabhakaran, M. P., Zamani, M., Felice, B., & Ramakrishna, S. (2015). Electrospraying technique for the fabrication of metronidazole contained PLGA particles and their release profile. Materials Science and Engineering: C, 56, 66-73, doi: 10.1016/j.msec.2015.06.018.

[9] Malli, S., Bories, C., Ponchel, G., Loiseau, P. M., & Bouchemal, K. (2018). Phase solubility studies and anti-Trichomonas vaginalis activity evaluations of metronidazole and methylated β-cyclodextrin complexes: Comparison of CRYSMEB and RAMEB. Experimental parasitology, 189, 72-75, doi: 10.1016/j.exppara.2018.04.019.

[10] Bensouiki, S., Belaib, F., Sindt, M., Rup-Jacques, S., Magri, P., Ikhlef, A., & Meniai, A. H. (2022). Synthesis of cyclodextrins-metronidazole inclusion complexes and incorporation of metronidazole-2-hydroxypropyl-β-cyclodextrin inclusion complex in chitosan nanoparticles. Journal of Molecular Structure, 1247, 131298, doi: 10.1016/j.molstruc.2021.131298.

[11] Celebioglu, A., & Uyar, T. (2019). Metronidazole/Hydroxypropyl-β-Cyclodextrin inclusion complex nanofibrous webs as fast-dissolving oral drug delivery system. International Journal of Pharmaceutics, 572, 118828, doi: 10.1016/j.ijpharm.2019.118828.

[12] Zhao, Y., & Truhlar, D. G. (2005). Design of density functionals that are broadly accurate for thermochemistry, thermochemical kinetics, and nonbonded interactions. The Journal of Physical Chemistry A, 109(25), 5656-5667, doi: 10.1021/jp050536c.

[13] Stephens, P. J., Devlin, F. J., Chabalowski, C. F., & Frisch, M. J. (1994). Ab initio calculation of vibrational absorption and circular dichroism spectra using density functional force fields. The Journal of physical chemistry, 98(45), 11623-11627, doi: 10.1021/j100096a001.

[14] Kim, S., Chen, J., Cheng, T., Gindulyte, A., He, J., He, S., ... & Bolton, E. E. (2021). PubChem in 2021: new data content and improved web interfaces. Nucleic acids research, 49(D1), D1388-D1395, doi: 10.1093/nar/gkaa971, doi: 10.1093/nar/gkaa971.

[15] HyperChem(TM) Professional 8.0, Hypercube, Inc., 1115 NW 4th Street, Gainesville, Florida 32601, USA.

[16] Frisch, M. E.; Trucks, G. W.; Schlegel, H. B.; Scuseria, G. E.; Robb, M. A.; Cheeseman, J. R.; Fox, D. J. Gaussian 16, revision C. 01. 2016.

[17] Dennington, R.; Keith, T. A.; Millam, J. M. GaussView, version 6.0. 16. Semichem Inc Shawnee Mission KS. 2016.

[18] Lu T, Chen F (2012) Multiwfn: a multifunctional wavefunction analyzer. J Comp Chem 33:580–592.

[19] Humphrey W, Dalke A, Schulten K (1996) VMD: visual molecular dynamics. J Molec Graphics 14:33–38.

[20] Song, K. S., Liu, L., Li, X. S., & Guo, Q. X. (2000). PM3 calculations on the complexation of α-cyclodextrin with the ground and excited quinone. Research on Chemical Intermediates, 26, 319-325, doi: 10.1163/156856700X00273.

[21] Stewart, J. J. (1989). Optimization of parameters for semiempirical methods II. Applications. Journal of computational chemistry, 10(2), 221-264, doi: 10.1002/jcc.540100209.

[22] Jenita, M. J., Prabhu, A., & Rajendiran, N. (2012). Theoretical study of inclusion complexation of tricylic antidepressant drugs with β-cyclodextrin.

[23] Rafati, A. A., Hashemianzadeh, S. M., Nojini, Z. B., & Safarpour, M. A. (2007). Theoretical study of the inclusion complexes of α and β-cyclodextrins with decyltrimethylammonium bromide (DTAB) and tetradecyltrimethylammonium bromide (TTAB). Journal of molecular liquids, 135(1-3), 153-157, doi: 10.1016/j.molliq.2006.11.006.

[24] Safia, H., Ismahan, L., Abdelkrim, G., Mouna, C., Leila, N., & Fatiha, M. (2019). Density functional theories study of the interactions between host β-Cyclodextrin and guest 8-Anilinonaphthalene-1-sulfonate: Molecular structure, HOMO, LUMO, NBO, QTAIM and NMR analyses. Journal of Molecular Liquids, 280, 218-229, doi: 10.1016/j.molliq.2019.01.019.

[25] Ohashi, M., Kasatani, K., Shinohara, H., & Sato, H. (1990). Molecular mechanics studies on inclusion compounds of cyanine dye monomers and dimers in cyclodextrin cavities. Journal of the American Chemical Society, 112(15), 5824-5830, doi: 10.1021/ja00171a023.

[26] Belhouchet, H. R., Abbaz, T., Bendjedou, A., Gouasmia, A., & Villemin, D. (2022). A computational study of the inclusion of β-cyclodextrin and nicotinic acid: DFT, DFT-D, NPA, NBO, QTAIM, and NCI-RDG studies. Journal of Molecular Modeling, 28(11), 348, doi: 10.1007/s00894-022-05342-1.

[27] Bouhadiba, A., Belhocine, Y., Rahim, M., Djilani, I., Nouar, L., & Khatmi, D. E. (2017). Host-guest interaction between tyrosine and β-cyclodextrin: Molecular modeling and nuclear studies. Journal of Molecular Liquids, 233, 358-363, doi: 10.1016/j.molliq.2017.03.029.

[28] Barbiric, D. J., Castro, E. A., & De Rossi, R. H. (2000). A molecular mechanics study of 1: 1 complexes between azobenzene derivatives and β-cyclodextrin. Journal of Molecular Structure: THEOCHEM, 532(1-3), 171-181, doi: 10.1016/S0166-1280(00)00516-9.

[29] Senthil Raj, P., Periandy, S., Xavier, S., & Attia, M. I. (2017). Molecular structure, vibrational spectra, HOMO, LUMO and NMR studies of methylphenylcyclopropenone based on density functional theories. In Recent Trends in Materials Science and Applications: Nanomaterials, Crystal Growth, Thin films, Quantum Dots, & Spectroscopy (Proceedings ICRTMSA 2016) (pp. 655-683). Springer International Publishing, doi: 10.1007/978-3-319-44890-9_55.

[30] Gümüş, H. P., Tamer, Ö., Avcı, D., & Atalay, Y. (2014). Quantum chemical calculations on the geometrical, conformational, spectroscopic and nonlinear optical parameters of 5-(2-Chloroethyl)-2, 4-dichloro-6-methylpyrimidine. Spectrochimica Acta Part A: Molecular and Biomolecular Spectroscopy, 129, 219-226, doi: 10.1016/j.saa.2014.03.031.

[31] Nora, M., Ismahan, L., Abdelkrim, G., Mouna, C., Leila, N., Fatiha, M., ... & Brahim, H. (2020). Interactions in inclusion complex of β-cyclodextrin/l-Metheonine: DFT computational studies. Journal of Inclusion Phenomena and Macrocyclic Chemistry, 96, 43-54, doi: 10.1007/s10847-019-00948-0.

[32] Venkataramanan, N. S., Suvitha, A., & Kawazoe, Y. (2019). Unraveling the binding nature of hexane with quinone functionalized pillar [5] quinone: a computational study. Journal of Inclusion Phenomena and Macrocyclic Chemistry, 95(3), 307-319, doi: 10.1007/s10847-019-00945-3.

[33] Ramalingam, S., Periandy, S., Karabacak, M., & Karthikeyan, N. (2013). Spectroscopic (FT-IR/FT-Raman) and computational (HF/DFT) investigation and HOMO/LUMO/MEP analysis on 2-amino-4-chlorophenol. Spectrochimica Acta Part A: Molecular and Biomolecular Spectroscopy, 104, 337-351, doi: 10.1016/j.saa.2012.11.107.

[34] Asiri, A. M., Karabacak, M., Kurt, M., & Alamry, K. A. (2011). Synthesis, molecular conformation, vibrational and electronic transition, isometric chemical shift, polarizability and hyperpolarizability analysis of 3-(4-Methoxy-phenyl)-2-(4-nitro-phenyl)-acrylonitrile: a combined experimental and theoretical analysis. Spectrochimica Acta Part A: Molecular and Biomolecular Spectroscopy, 82(1), 444-455, doi: 10.1016/j.saa.2011.07.076.

[35] Schreckenbach, G., & Ziegler, T. (1995). Calculation of NMR shielding tensors using gauge-including atomic orbitals and modern density functional theory. The Journal of Physical Chemistry, 99(2), 606-611, doi: 10.1021/j100002a024.

[36] Pulay, P., & Hinton, J. F. (2007). Shielding theory: GIAO method. eMagRes, doi: 10.1002/9780470034590.emrstm0501.

[37] Reed, A. E., Curtiss, L. A., & Weinhold, F. (1988). Intermolecular interactions from a natural bond orbital, donor-acceptor viewpoint. Chemical Reviews, 88(6), 899-926, doi: 10.1021/cr00088a005.

[38] Prabhu, M. D., Yenagi, J. T., Kamat, V., & Tonannavar, J. (2020). XRD structure and vibrational analysis of DL-β-Leucine, as aided by DFT tetramer model and characterized by NBO, AIM and NCI calculations. Journal of Molecular Structure, 1218, 128495, doi: 10.1016/j.molstruc.2020.128495.

[39] Chen, H., & Ji, H. (2010). Alkaline hydrolysis of cinnamaldehyde to benzaldehyde in the presence of β-cyclodextrin. AIChE journal, 56(2), 466-476, doi: 10.1002/aic.12017.

[40] Zaboli, M., & Raissi, H. (2015). The analysis of electronic structures, adsorption properties, NBO, QTAIM and NMR parameters of the adsorbed hydrogen sulfide on various sites of the

outer surface of aluminum phosphide nanotube: a DFT study. Structural Chemistry, 26, 1059-1075, doi: 10.1007/s11224-015-0563-2.

[41] Bader Richard, F. W. (1994). Atoms in Molecules: A Quantum Theory.

[42] Venkataramanan, N. S., Suvitha, A., & Kawazoe, Y. (2017). Intermolecular interaction in nucleobases and dimethyl sulfoxide/water molecules: A DFT, NBO, AIM and NCI analysis. Journal of molecular graphics and modelling, 78, 48-60, doi: 10.1016/j.jmgm.2017.09.022.

[43] Bader, R. F. (2006). Comment on: Revisiting the variational nature of the quantum theory of atoms in molecules. Chemical physics letters, 426(1-3), 226-228, doi: 10.1016/j.cplett.2006.05.072.

[44] Becke, A. (2007). The quantum theory of atoms in molecules: from solid state to DNA and drug design. John Wiley & Sons.

[45] Espinosa, E., Molins, E., & Lecomte, C. (1998). Hydrogen bond strengths revealed by topological analyses of experimentally observed electron densities. Chemical physics letters, 285(3-4), 170-173, doi: 10.1016/S0009-2614(98)00036-0.

[46] Bader, R. F. (1985). Atoms in molecules. Accounts of chemical research, 18(1), 9-15, doi: 10.1021/ar00109a003.

[47] Nkungli, N. K., & Ghogomu, J. N. (2017). Theoretical analysis of the binding of iron (III) protoporphyrin IX to 4-methoxyacetophenone thiosemicarbazone via DFT-D3, MEP, QTAIM, NCI, ELF, and LOL studies. Journal of Molecular Modeling, 23, 1-20, doi: 10.1007/s00894-017-3370-4.

[48] Richard, F., & Bader, R. (1990). Atoms in molecules: a quantum theory.

[49] Koch, U., & Popelier, P. L. (1995). Characterization of CHO hydrogen bonds on the basis of the charge density. The Journal of Physical Chemistry, 99(24), 9747-9754, doi: 10.1021/j100024a016.

[50] Nakanishi, W., Hayashi, S., & Narahara, K. (2008). Atoms-in-molecules dual parameter analysis of weak to strong interactions: behaviors of electronic energy densities versus Laplacian of electron densities at bond critical points. The Journal of Physical Chemistry A, 112(51), 13593-13599, doi: 10.1021/jp8054763.

[51] Nakanishi, W., Hayashi, S., & Narahara, K. (2009). Polar Coordinate Representation of H b (rc) versus ($\hbar$2/8 m)∇ 2ρb (rc) at BCP in AIM Analysis: Classification and Evaluation of Weak to Strong Interactions. The Journal of Physical Chemistry A, doi: 10.1021/jp903622a.

[52] Rozas, I., Alkorta, I., & Elguero, J. (2000). Behavior of ylides containing N, O, and C atoms as hydrogen bond acceptors. Journal of the American Chemical Society, 122(45), 11154-11161, doi: 10.1021/ja0017864.

[53] Venkataramanan, N. S., & Suvitha, A. (2018). Nature of bonding and cooperativity in linear DMSO clusters: a DFT, AIM and NCI analysis. Journal of Molecular Graphics and Modelling, 81, 50-59, doi: 10.1016/j.jmgm.2018.02.010.

[54] Zahedi, E., Shaabani, S., & Shiroudi, A. (2017). Following the molecular mechanism of decarbonylation of unsaturated cyclic ketones using bonding evolution theory coupled with NCI analysis. The Journal of Physical Chemistry A, 121(44), 8504-8517, doi: 10.1021/acs.jpca.7b08503.

[55] Tahenti, M., Gatfaoui, S., Issaoui, N., Roisnel, T., & Marouani, H. (2020). A tetrachlorocobaltate (II) salt with 2-amino-5-picolinium: Synthesis, theoretical and experimental characterization. Journal of Molecular Structure, 1207, 127781, doi: 10.1016/j.molstruc.2020.127781.

[56] Saleh, G., Gatti, C., Lo Presti, L., & Contreras-García, J. (2012). Revealing non-covalent interactions in molecular crystals through their experimental electron densities. Chemistry–A European Journal, 18(48), 15523-15536, doi: 10.1002/chem.201201290.

[57] Meryem, G., Rabah, K., Fatiha, M., Leila, N., Aziz, B. A., Imane, D., & Rachid, M. (2021). Computational investigation of vanillin@ βéta-cyclodextrin inclusion complex: Electronic and intermolecular analysis. Journal of Molecular Liquids, 321, 114839, doi: 10.1016/j.molliq.2020.114839.

[58] Lefebvre, C., Rubez, G., Khartabil, H., Boisson, J. C., Contreras-García, J., & Hénon, E. (2017). Accurately extracting the signature of intermolecular interactions present in the NCI plot of the reduced density gradient versus electron density. Physical Chemistry Chemical Physics, 19(27), 17928-17936, doi: 10.1039/C7CP02110K.

[59] Lefebvre, C., Khartabil, H., Boisson, J. C., Contreras-García, J., Piquemal, J. P., & Hénon, E. (2018). The independent gradient model: a new approach for probing strong and weak interactions in molecules from wave function calculations. ChemPhysChem, 19(6), 724-735, doi: 10.1002/cphc.201701325.

[60] Lu, T. (2020). Multiwfn Manual, version 3.7 (dev), Section 4.8. 5.

[61] Yan, X., Wang, Y., Meng, T., & Yan, H. (2021). Computational insights into the influence of substitution groups on the inclusion complexation of β-cyclodextrin. Frontiers in Chemistry, 9, 668400, doi: 10.3389/fchem.2021.668400.